Inducing locally structured ion energy distributions in intermediate-pressure plasmas

Scott J. Doyle[1], Andrew R. Gibson[1,2,3], Rod W. Boswell[4], Christine Charles[4], and James P. Dedrick[1]

[1]York Plasma Institute, Department of Physics, University of York, Heslington, York, YO10 5DD, UK

[2]Research Group for Biomedical Plasma Technology, Ruhr-Universität Bochum, Universitätsstraße 150, 44801 Bochum, Germany

[3]Institute of Electrical Engineering and Plasma Technology, Ruhr-Universität Bochum, Universitätsstraße 150, 44801 Bochum, Germany

[4]Space Plasma, Power and Propulsion Laboratory, Research School of Physics and Engineering, The Australian National University, ACT 2601, Australia

[1]E-mail: Scott.Doyle@Physics.org

June 21, 2019

Abstract

Ion energy distribution functions (IEDFs) incident upon material surfaces in radio-frequency capacitively coupled plasmas (rf CCPs) are coupled to the spatial and temporal sheath dynamics. Tailoring the ion energy distribution function within intermediate-pressure plasmas ($\approx$ 133 Pa, 1 Torr), finding application in surface modification and aerospace industries, is challenging due to the collisional conditions. In this work, experimentally benchmarked fluid/Monte-Carlo simulations are employed to demonstrate the production of structured IEDFs in a collisional (200 Pa 1.5 Torr argon) rf hollow cathode discharge. The formation of structures within the IEDFs is explained by an increase in the Ar^+ ion-neutral mean-free-path and simultaneous decrease in the phase-averaged sheath extension as the rf voltage frequency increases over 13.56 - 108.48 MHz for a constant rf voltage amplitude (increasing plasma power) and gas flow rate. Two distinct transitions in the shape of the IEDF are observed at 450 V, corresponding to the formation of 'mid-energy' (60 - 180 eV) structures between 40.68 - 54.24 MHz and additional 'high energy' ($\gtrsim$ 180 eV) structures between 81.36 - 94.92 MHz, the structures within each region displaying a distinct sensitivity to the applied

voltage amplitude. Transitions between these energy ranges occurred at lower applied voltages for increased applied voltage frequencies, providing increased control of the mean and modal ion energy over a wider voltage range. Capability to extend the range of access to an operational regime where the structured IEDFs are observed is desirable for applications that require control of the ion-bombardment energy under collisional plasma conditions.

1 Introduction

The enhancement of capacitively coupled plasma (CCP) sources through the implementation of hollow cathode (HC) geometries represents an area of recent interest[1–4]. Applications of HC sources range from scalable arrays for homogeneous surface modification[5,6] to micro-discharge sources for spacecraft propulsion[7–9]. Control of the ion energy distribution function (IEDF) throughout the plasma has been found to be important for these applications[1,10]. For example, in the semiconductor industry the IEDF incident upon material surfaces plays a crucial role in the quality and homogeneity of etching and deposition processes[6,11]. Ions that are accelerated through sheaths adjacent to plasma facing surfaces impact the wall with an energy distribution that is dependant upon the ion-neutral collision frequencies, the phase-averaged sheath width and the sheath potential[12]. The resulting mean and modal ion-bombardment energies can therefore be significantly affected by the amplitude and frequency of the applied voltage waveform[13].

Structured IEDFs differ from unstructured distributions as they exhibit additional characteristic peaks, typically associated with the radio-frequency modulation of the sheath potential[14].Previous works related to structured IEDFs in rf plasmas were primarily focused over the range from low to intermediate pressure discharges (0.65 - 67 Pa, 5 - 500 mTorr) at applied voltage frequencies of 13.56 MHz[14–17] and 27.12 MHz[18]. More recent work has demonstrated control of the IEDF in low-pressure (0.65 - 1.3 Pa, 5 - 10mTorr) plasmas through application of higher applied voltage frequencies in the range 12 MHz - 100 MHz[12,19,20]. For applications involving higher-pressure discharges (above 200 Pa, 1.5 Torr) the increased ion-neutral collision frequency results in a collisionally dominated IEDF at the wall, the shape of which is largely independent of the voltage amplitude, limiting the range of accessable ion energies[12]. At these pressures, heating and rarefaction of the neutral gas plays a substantial role in determining the heavy particle collision rates and mean-free-paths[21,22]. Therefore, to adequately model the IEDF at these pressures, it is necessary to self consistently solve for the change in neutral gas density that mediates the transfer of energy through ion-neutral collisions.

In this work, the formation of structured IEDFs with increasing driving frequency (13.56 - 108.48 MHz) in a collisional (200 Pa, 1.5 Torr argon) capacitively coupled hollow-cathode microdischarge is investigated through the application of an experimentally validated two-dimensional fluid/Monte-Carlo model. A brief description of the experimental set up and numerical model are given in section 2. Agreement between the measured and simulated Ar($2p_1$ - $1s_2$) electron impact excitation rates is demonstrated for 13.56 MHz, 27.12 MHz and 40.68 MHz applied voltage frequencies at 450 V applied voltage in section 3. Additional simulations are employed to draw conclusions up to 108.48 MHz, where the evolution of the IEDFs with respect to applied voltage amplitude and frequency is presented in

section 4. The corresponding variation in the Ar^+ mean-free-path and radial sheath extension, and how these drive the formation of the structured IEDFs, is discussed in section 5.

2 Experimental Method and Simulation Model

The hollow cathode microdischarge source, shown in figure 1, employs an annular powered electrode surrounding a 4.2 mm inner-diameter alumina tube through which 100 sccm of argon gas is supplied[23–29]. During steady-state operation, an axial pressure gradient exists between the plenum at 200 Pa (1.5 Torr) and expansion region at 113 Pa (0.85 Torr).

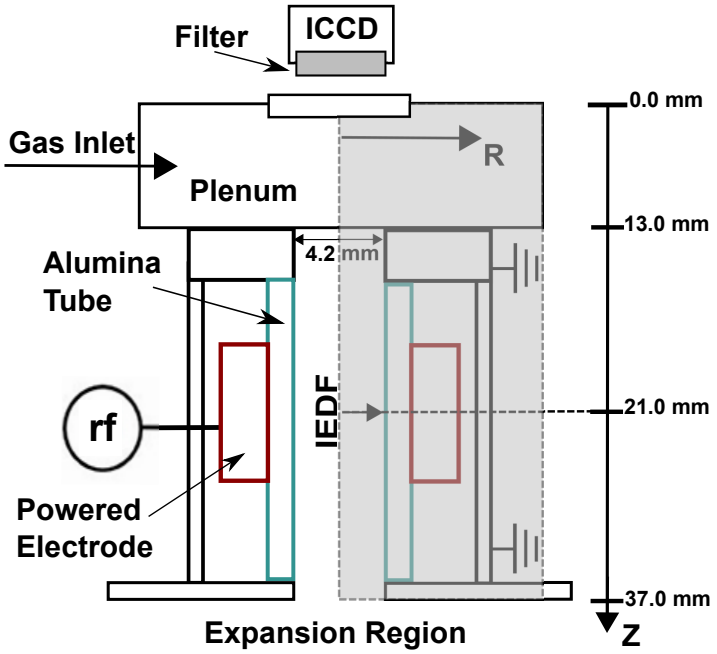

Figure 1: Schematic of the experimental setup (not to scale), where the simulated region is denoted by the shaded grey area. The imaging plane of the ICCD camera is centered on the midplane of the powered electrode ($Z = 21$ mm). Simulated IEDFs are obtained from Ar^+ ions incident on the radial wall (R, $Z = 2.1$ mm, 21 mm) as denoted by the solid arrow.

In the experiment, power is supplied via an arbitrary waveform generator (Keysight 33621A, 120 MHz), broadband amplifier (IFI SCCX100, 0.01 - 220 MHz) and matching network connected in series with the powered electrode. The grounded electrode area in contact with the plasma exceeds the powered electrode area. Therefore, to maintain current continuity through both the powered and grounded surfaces, a dc self-bias voltage forms on the surface of the alumina wall adjacent to the powered electrode[30,31]. Argon ions are accelerated radially through the sheath adjacent to the powered electrode and undergo ion-neutral charge exchange collisions, resulting in significant neutral gas heating within the powered electrode sheath[21,22,25,32]. Secondary electrons, released through positive ion bombardment, are accelerated back into the plasma bulk at high, non-thermal energies (above 50 eV), representing an efficient additional ionisation mechanism[33,34].

Two-dimensional, fluid-kinetic simulations were undertaken using the Hybrid Plasma Equipment Model (HPEM)[35]. A full description of the mesh and numerical methods applied can be found in Refs. 22 and 36, a summary is provided here. The simulated region is shown in figure 1 as the shaded grey area. The simulation mesh consisted of a rectilinear grid of 64 $\times$ 152 (R $\times$ Z) cells in a cylindrically symmetric geometry, corresponding to a radial resolution of 0.125 mm per cell and an axial resolution of 0.5 mm per cell. A higher radial resolution was employed to enable a discussion of the phase-resolved sheath dynamics perpendicular to the dielectric surface. The sheath extension is calculated as in Ref. 36, where the radial sheath edge S_R is determined as the radius R that satisfies the Brinkmann criterion[37].

Species considered within the model are Ar, Ar(4s), Ar(4p), Ar(4d), Ar_2^*, Ar^+, Ar_2^+ and e^-, where the reaction mechanism is as discussed in Ref. 38. Gas-phase electron-neutral and electron-ion collisions include elastic, excitation and ionisation reactions[38]. Cascade processes, multi-step ionisation and heavy particle mixing between excited species are also included, the interaction cross-sections for which are obtained from Refs. 39–43. Ion-neutral charge exchange collisions are employed with a rate coefficient of 5.66×10^{-10} cm^{-3} s^{-1} $(T_g/300)^{0.5}$ where T_g is the neutral-gas temperature[44]. The energy distribution functions for all gas-phase heavy particle species are assumed to be Maxwellian and are obtained from a two-term approximation of the Boltzmann equation. Ion energy distributions for Ar^+ incident on the radial wall at (R, Z = 2.1 mm, 21 mm) are obtained via a kinetic Monte-Carlo algorithm employing the same reaction mechanism as used in the gas phase[35].

Phase-resolved optical emission spectroscopy (PROES)[45,46] was performed to enable a comparison of the measured and simulated electron heating mechanisms, and hence also the phase-resolved sheath dynamics. For further details see Ref. 22. Images were acquired with an ICCD camera (Andor iStar DH344T-18U-73, 1024 $\times$ 1024 array, pixel size: 13 $\times$ 13 μm^2) employing an optical gate width of 1.7 ns and a 750.466 nm bandpass filter (LOT-QuantumDesign, 1 nm FWHM). A depth of field of 24 mm, corresponding to the axial length of the source region, was applied to the simulated PROES images through a top hat integration along the line of sight[47]. Previous work has demonstrated agreement between the measured and simulated phase-resolved, Ar($2p_1$) electron impact excitation rates in this source[22,36]. Here, experimental comparisons are presented for 13.56 MHz, 27.12 MHz and 40.68 MHz applied voltage frequencies at an applied voltage amplitude of ϕ_{rf} = 450 V. Additional simulations are employed to draw conclusions up to 108.48 MHz.

3 Electron-Impact Excitation Rate: Simulations and Experiments

The measured and simulated Ar($2p_1$) excitation rates for 13.56 MHz, 27.12 MHz and 40.68 MHz driving frequency discharges at 450 V applied voltage amplitude are shown in figure 2.

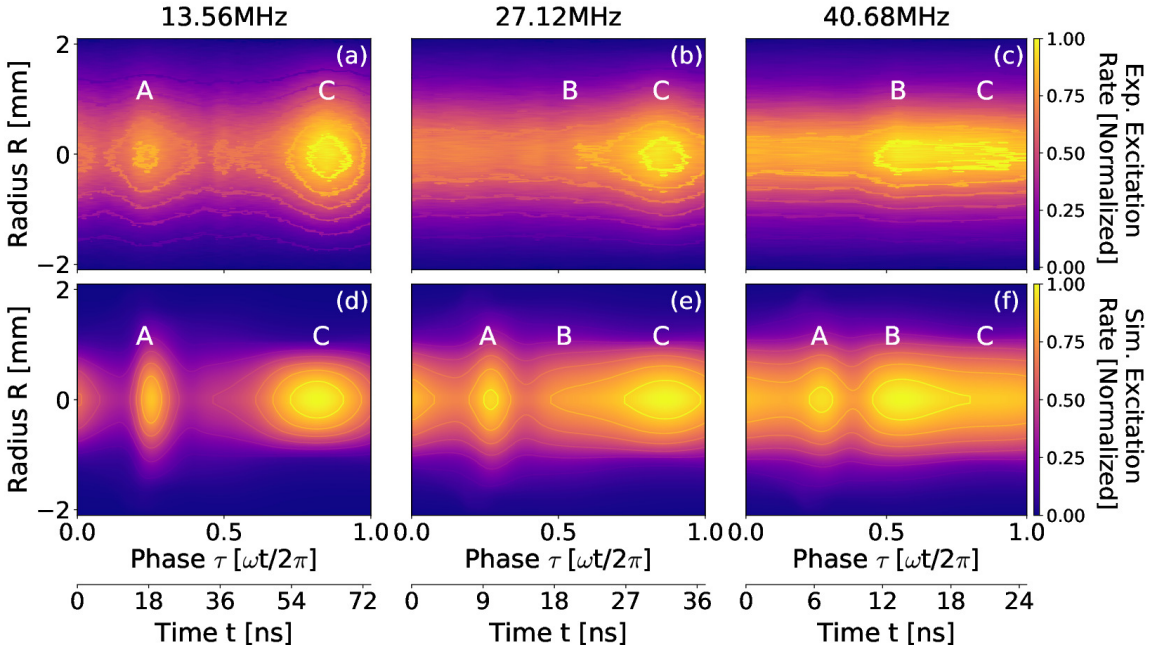

Figure 2: Ar($2p_1$) excitation rates for 13.56 MHz, 27.12 MHz and 40.68 MHz applied voltage frequencies as measured experimentally (a-c), and via simulation (d-f). Plenum pressure 200 Pa (1.5 Torr) argon, applied voltage $\phi_{\mathrm{rf}} = 450$ V.

At 13.56 MHz, (figures 2 (a) and (d)), close agreement is observed between simulation and experiment and a similarly high level of agreement is observed over a wider voltage range of 150 - 450 V (not shown), representing the full operational range of the experiment. Here, peak A represents electron heating due to the collapsing sheath edge[48], while peak C represents secondary electron impact excitation[49] at the phase of most negative dielectric surface potential, $\tau = 0.75$.

Similar spatio-temporal heating mechanisms are observed for 27.12 MHz, shown in figures 2 (b) and (e). Secondary electron excitation (peak C) remains the dominant electron heating mechanism in both the measurement and simulation. Sheath expansion heating[50] (peak B) is observed in both simulation and experiment over the phase interval $0.4 \leq \tau \leq 0.7$. Although close agreement is observed between simulation and experiment at 27.12 MHz for peaks B and C, sheath collapse heating (peak A) is overestimated in the simulation. The degree of excitation during sheath collapse is proportional to the mean electron velocity out of the plasma bulk, where the total electron flux during the phase of sheath collapse must balance the positive ion loss during phases where the sheath extent is greater than zero[30]. For a given electron-neutral collision frequency, a reduction in the electron density will enforce an increase in the average electron velocity to maintain the same flux. Therefore, the overestimation in sheath collapse heating may indicate an underestimated plasma density in the simulation as compared

to the experiment[51,52].

As the driving frequency is increased to 40.68 MHz, the dominant electron heating mechanism shifts from secondary electron heating (peak C) to sheath expansion heating (peak B), shown in figures 2 (c) and (f). This transition occurs as sheath expansion heating is dependant upon the expanding sheath velocity, which increases with increasing driving frequency. In contrast, the reduction in the secondary electron excitation arises from a reduction in the absolute time for which the sheath is fully extended. Sheath collapse heating (peak A) remains overestimated through the same reasoning as for 27.12 MHz. Sheath expansion heating and heating via secondary electrons are less sensitive to changes in the plasma density as they are to variations in the sheath dynamics[48]. Therefore, as close agreement is observed between simulation and experiment with respect to sheath expansion and secondary electron heating, and their transition at 40.68 MHz, it may be inferred that the phase-resolved sheath dynamics are being modelled appropriately. Note that an underestimation of the Ar^+ ion density will likely result in a slight systematic overestimation of the sheath extent[31].

4 Evolution of Ion Energy Distribution Functions

Figure 3 shows the evolution of the Ar^+ IEDFs incident on the alumina wall adjacent to the powered electrode (R, Z = 2.1 mm, 21 mm) with respect to applied voltage for 13.56 - 108.48 MHz over the voltage range 150 - 450 V.

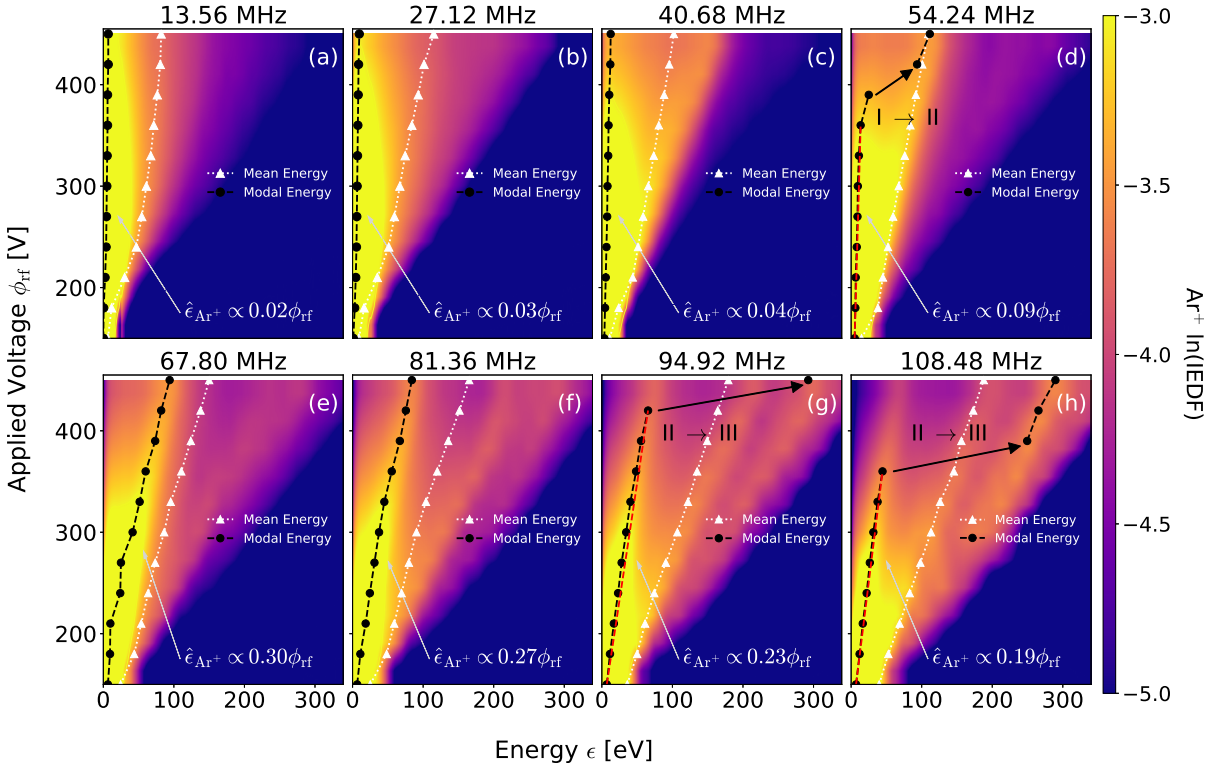

Figure 3: Ar^+ ion energy distribution functions incident on the dielectric radial wall adjacent to the powered electrode (R, Z = 2.1 mm, 21 mm, see figure 1), for applied voltage amplitudes of 150 - 450 V and applied voltage frequencies of 13.56 - 108.48 MHz, (a-h). The mean and modal $\hat{\epsilon}_{Ar^+}$ ion energies are indicated by dotted and dashed lines, respectively, where discontinuous transitions in the modal Ar^+ energy are denoted by the black arrows in panels (d), (g) and (h). The modal energy proportionalities to the applied voltage are obtained from linear fits over the full voltage range, with the exception of 54.24 MHz, 94.92 MHz and 108.48 MHz, which are performed over the voltage ranges 150 - 360 V, 150 - 420 V and 150 - 360 V, respectively, as denoted by the red dashed lines in the associated panels. The colourbar scale has been reduced, omitting IEDF fractions above 10^{-3} and below 10^{-5} for clarity. Plenum pressure 200 Pa (1.5 Torr) argon, ϕ_{rf} = 150 - 450 V.

In figure 3, the mean and modal $\hat{\epsilon}_{Ar^+}$ ion energies are denoted by the black and white lines, respectively. Here, the modal ion energy represents the most populous structure within the distribution, while the mean more generally characterises the entire distribution. The 13.56 MHz IEDFs in figure 3 (a) exhibit profiles where the majority of Ar^+ ions are maintained at low energies (0.6 eV $\leq \hat{\epsilon}_{Ar^+} \leq$ 6 eV), supplemented by a high energy (50 - 200 eV) tail containing relatively few ions. This structure is expected for the relatively high pressure (200 Pa, 1.5 Torr) discharge conditions, where the ion-neutral collision frequency is high[10,12,53]. As a result, the mean and modal ion energies exhibit little change

with varying applied voltage amplitude. Note however, that an increase in the fraction of ions within the high energy tail is observed with increasing applied voltage amplitude.

Increasing the driving frequency to 27.12 MHz, figure 3 (b), results in much the same behaviour as observed for the 13.56 MHz case. The first notable change in the shape of the IEDFs occurs between 40.68 MHz and 54.24 MHz, figures 3 (c) and (d), respectively, where the IEDFs exhibit an additional mid-energy ($\approx$ 60 - 180 eV) structure in addition to the low energy ($\leq$ 60 eV) structure observed previously. The modal ion energy transitions into this structure for applied voltage amplitudes above 390 V at 54.24 MHz, denoted by "I $\rightarrow$ II" in figure 3 (d), representing a distinct transition in the distribution of energies within the IEDF.

For applied voltage frequencies of 67.80 MHz and 81.36 MHz, figures 3 (e) and (f), the modal ion energy sits within the mid-energy structure for almost the entire voltage range. This represents an increased sensitivity of the modal ion energy to the applied voltage amplitude. In addition, an increase in the fraction of ions within the high energy tail of the distribution ($\gtrsim$ 180 eV) is observed. The high energy tail begins to stratify into two further structures, positioned either side of the mean energy of the distribution, for applied voltage frequencies of 94.92 MHz and 108.48 MHz in figures 3 (g) and (h). Here, a structure refers to a sub-component of the IEDF that can be best approximated via a Gaussian or Lorentzian distribution as opposed to a Maxwell-Boltzmann distribution. The fraction of ions within these structures increases in proportion to the applied voltage amplitude, until the modal ion energy exhibits a transition into the highest energy structure at 450 V for 94.92 MHz ("II $\rightarrow$ III" in figure 3 (g)). This transition occurs at a lower voltage of 390 V for 108.48 MHz.

The trends observed in figures 3 (a - h) indicate the formation of 'mid-energy' ($\approx$ 60 - 180 eV) and 'high energy' ($\gtrsim$ 180 eV) structures (II and III, respectively) in the IEDFs, the formation and evolution of which vary with both the driving frequency and amplitude. To further characterise these structures, the IEDFs incident on the alumina wall adjacent to the powered electrode (R, Z = 2.1 mm, 21 mm), for varying applied voltage frequencies between 13.56 - 108.48 MHz at an applied voltage amplitude of 450 V, are shown in figure 4.

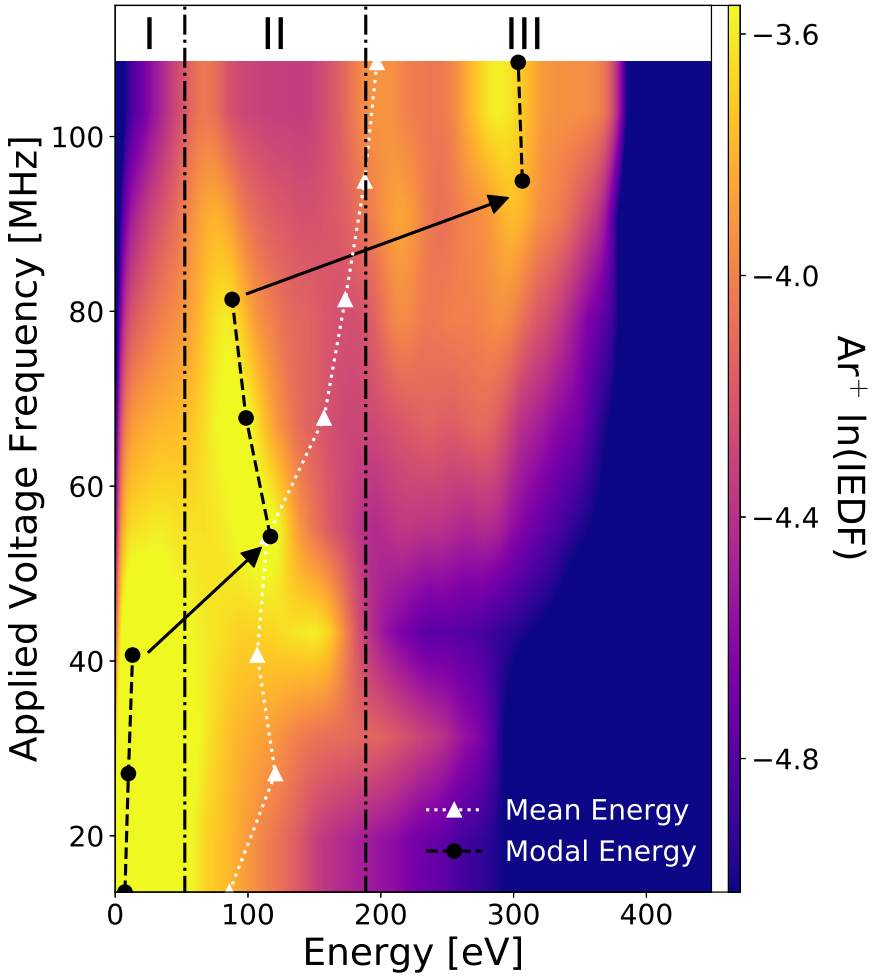

Figure 4: Ar^+ ion energy distribution functions incident on the dielectric radial wall adjacent to the powered electrode (R, Z = 2.1 mm, 21 mm, see figure 1), for applied voltage frequencies between 13.56 - 108.48 MHz and an applied voltage amplitude of 450 V. The modal $\hat{\epsilon}_{Ar^+}$ and mean Ar^+ ion energies are denoted by the black dashed and white dotted lines, respectively. The IEDFs can be broadly described by structures in three energy regions, seperated by the dash-dotted lines, which correspond to: I (0 - 60 eV), II (60 - 180 eV) and III ($\geq$ 180 eV). For clarity, the colourbar dynamic scale has been reduced, omitting IEDF fractions below 10^{-5}. Plenum pressure 200 Pa (1.5 Torr) argon, 450 V applied voltage amplitude.

The structures within the IEDFs presented in figure 4 can be categorised into three energy ranges: Region I (0 - 60 eV) contains the largest fraction of ions for applied voltage frequencies between 13.56 - 40.68 MHz. This region consists primarily of low energy ions where the modal ion energy $\hat{\epsilon}_{Ar^+}$ is far below the phase-averaged sheath potential ($\approx$ -350 V), indicating a regime in which this is determined primarily through the high ion-neutral collision frequency. Region II (60 - 180 eV) contains the largest fraction of the IEDF for applied voltage frequencies between 54.24 - 81.36 MHz, this structure becoming visible above 40.68 MHz. This region consists of a single 'mid-energy' structure, the magnitude of which increases until approximately 67.80 MHz, and decreases thereafter. The modal energy in this region is inversely proportional to the driving frequency, levelling off at $\approx$ 80 eV for frequencies above 94.92 MHz.

For applied voltage frequencies of 67.80 - 108.48 MHz two additional 'high energy' peaks begin to

form in region III, above 180 eV. The formation of these structures is observed for applied voltage frequencies above 67.80 MHz as a single broadband (80 eV energy range) structure, the centre of which approximately corresponds to 240 eV. The magnitude and energy range of this structure increases with increasing driving frequency. At and above 94.92 MHz, this structure stratifies into two distinct components, with the higher energy of the two components representing the modal Ar^+ ion energy. The formation of these discrete high-energy peaks represents an increasing fraction of ions exhibiting reduced collisional losses within the sheath volume.

The modal Ar^+ ion energy exhibits sharp transitions between regions I - II (40.68 - 54.24 MHz) and II - III (81.36 - 94.92 MHz), observed previously in figures 3 (d), (g) and (h). A variation of 280 eV in the modal ion energy $\hat{\epsilon}_{Ar^+}$ is achieved over the driving frequency range 13.56 -108.48 MHz. In comparison, the mean ion energy increases in proportion with the driving frequency, varying by 106 eV over the same frequency range. The mean energy exhibits an increased proportionality to the applied voltage amplitude at applied voltage frequencies between 54.24 - 108.36 MHz, correlating with the formation of the structured IEDFs. At 94.92 MHz and upwards the modal ion energy exceeds the mean ion energy as it transitions into region III, which increasingly represents the defining region of the IEDF.

5 Mechanism for the Formation Structured IEDFs

The formation of the structures observed previously in figures 4 and 5 (g) and (h), suggests a reduction in the ion-neutral collision frequency within the sheath. To investigate this, IEDFs incident upon the alumina wall (R, Z = 2.1 mm, 21 mm) for 13.56 MHz and 108.48 MHz applied-voltage frequencies and 150 V, 300 V and 450 V applied voltages are shown in figures 5 (a) and (b). The sheath averaged neutral argon density n_{Ar} and argon ion density $n_{\mathrm{Ar^+}}$ are shown with respect to driving frequency in figure 5 (c) and the associated $\mathrm{Ar^+}$ mean-free-path λ_{mfp} and phase-averaged sheath extent S_R are shown in figure 5 (d). The $\mathrm{Ar^+}$ mean-free-path was calculated by employing an Ar - $\mathrm{Ar^+}$ cross-section corresponding to the mean $\mathrm{Ar^+}$ ion velocity at the sheath edge, where the energy resolved cross-section was obtained from Ref. 54.

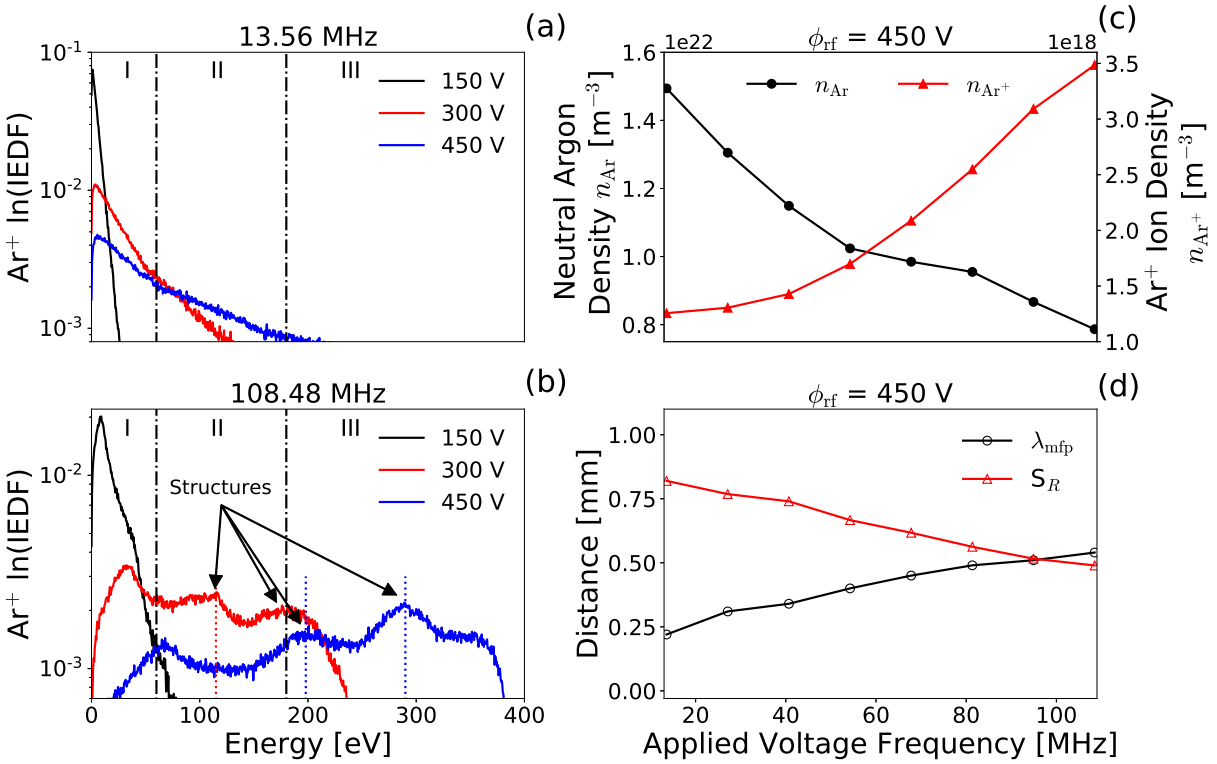

Figure 5: $\mathrm{Ar^+}$ ion energy distribution functions incident on the dielectric radial wall adjacent to the powered electrode (R, Z = 2.1 mm, 21 mm, see figure 1) for applied voltage frequencies of (a) 13.56 MHz and (b) 108.48 MHz and increasing voltage amplitude. Panels (c) and (d) show the effects of varying the driving frequency for a 450 V discharge on the (c) sheath averaged neutral argon n_{Ar} and argon ion $n_{\mathrm{Ar^+}}$ densities, and (d) $\mathrm{Ar^+}$ mean-free-path λ_{mfp} and phase-averaged sheath extent S_R. Energy regions I, II, and III are seperated by dash-dotted lines, while IEDF structures are denoted by dotted lines in (a) and (b). Plenum pressure 200 Pa (1.5 Torr) argon, ϕ_{rf} = 150 - 450 V.

The shape of the IEDFs at 13.56 MHz in figure 5 (a) are approximately independent of the applied voltage. The variation in the modal $\mathrm{Ar^+}$ ion energy at this frequency is predominately controlled by the neutral argon density (figure 5 (c)), which alters the ion-neutral collision rate. Increasing the applied voltage results in an increased maximum ion energy, while the modal energy, denoted by the

dashed lines, is not significantly affected (1.9 eV $\leq$ $\hat{\epsilon}_{Ar^+}$ $\leq$ 7.7 eV). Increasing the applied voltage primarily results in a broadening of the distribution function, resulting in a longer high-energy tail.

In contrast to 13.56 MHz, the shapes of the IEDFs at 108.48 MHz, shown in figure 5 (b), exhibit a strong dependence on the applied voltage. At 150 V the IEDF is similar to 13.56 MHz, where the relatively low modal Ar^+ ion energy ($\hat{\epsilon}_{Ar^+}$ = 9 eV) is dictated primarily by the high ion-neutral collision frequency and the majority of the distribution is within region I. Increasing the voltage from 150 V to 300 V results in a relatively flat distribution, now predominately within region II, exhibiting an increased modal Ar^+ ion energy of $\hat{\epsilon}_{Ar^+}$ = 34 eV and evidence of two additional higher energy structures between 60 - 180 eV. The central and most well defined structure at 108 eV is highlighted in figure 5 (b) by the red dotted line. At an applied voltage of 450 V the IEDF consists of three distinct structures, a relatively low-energy peak in region II at 88 eV and two additional higher energy structures in region III at 190 eV and 291 eV, denoted by the blue dotted lines. The modal Ar^+ ion energy has transitioned from the low-energy region I structure into the highest energy of the two region III structure and the distribution is now weighted towards the high energy ions as shown previously in figure 4. In this regime, the central energies at which the IEDF structures form are observed to be significantly influenced by the sheath potential via the dc self-bias voltage. The ion-neutral collision frequency within the sheath primarily determines the range of energies within these structures, i.e. their broadening. Note that the dc self-bias voltage ϕ_{dc} remains approximately constant over the range of applied voltage frequencies employed, varying between -303 V $\leq$ ϕ_{dc} $\leq$ 282 V at 450 V applied voltage amplitude.

The sheath averaged neutral argon and plasma densities are shown with respect to driving frequency in figure 5 (c) for an applied voltage of 450 V. Increasing the driving frequency for a fixed applied voltage increases the plasma density and reduces the neutral argon density. The neutral density decreases by approximately 50% from 13.56 MHz to 108.48 MHz. This rarefaction arises from increased neutral gas heating as the deposited power increases with driving frequency. A reduction in the neutral argon density reduces the Ar - Ar^+ collision frequency within the sheath, resulting in an increase in the Ar^+ mean-free-path, shown in figure 5 (d). While this increase in the mean-free-path can account for broadening of the IEDFs in figure 5 (a), it cannot independently account for the narrow and distinct structures observed in figure 5 (b). To describe the formation of these structures, the properties of the sheath adjacent to the powered electrode, through which ions are accelerated, is considered.

The variation in the phase-averaged sheath extension S_R with respect to driving frequency is shown in figure 5 (d). As noted previously, increasing the driving frequency leads to an increased Ar^+

density adjacent to the powered electrode, giving rise to a reduced sheath width and an increase in the sheath capacitance[31]. The negative dc self-bias voltage at the radial wall enforces an relatively phase-independent radial Ar^+ ion flux[31,36,55]. A reducing sheath extension, coupled with an increasing Ar^+ mean-free-path results in a reduced chance for ion-neutral collisions within the sheath volume as the driving frequency increases. Therefore, ion populations that are less influenced by collisions (region II) and effectively collisionless ion populations (region III) may be induced at relatively high (above 94.92 MHz at 1.5 Torr) applied voltage frequencies, enabling a greater degree of control of the range of energies within the IEDF.

6 Conclusions

To conclude, control of the shape of IEDFs incident on plasma facing material surfaces has been demonstrated via 2D fluid/Monte-Carlo simulations of a radio-frequency (13.56 - 108.48 MHz, 150 - 450 V) hollow cathode micro-discharge operating in argon at 200 Pa (1.5 Torr). Close agreement between simulation and experiment was observed over the range 13.56 - 40.68 MHz and a transition from collisional IEDFs to structured multi-peaked IEDFs exhibiting collisionless effects is observed for applied voltage frequencies above 54.24 MHz at 450 V in simulation. Two distinct transitions in the structure of the IEDF are observed at 450 V, corresponding to the formation of a single 'mid-energy' (90 - 150 eV) structure between 40.68 - 54.24 MHz, and two additional 'high energy' ($\approx$ 210 eV, $\approx$ 290 eV) structures which form at frequencies above 81.36 MHz. A significant degree of control of the mean and modal Ar^+ energies is achieved, varying by 106 eV and 280 eV, respectively. The formation of high energy structures within the IEDFs is attributed to the Ar - Ar^+ mean-free-path increasing beyond the phase-averaged sheath extent as the driving frequency is increased between 13.56 - 108.48 MHz. Supported by self-consistent modelling of the neutral gas temperature, the increased Ar - Ar^+ mean-free-path is explained by a reduction in the neutral gas density localised to the region adjacent to the powered electrode as a result of gas heating. Inducing structured IEDFs through application of higher applied voltage frequencies enables enhanced control of the ion-bombardment energy via the applied voltage amplitude under collisional plasma conditions.

7 Acknowledgments

The authors wish to thank M. J. Kushner for provision of the HPEM code and ongoing support, T. Gans and D. O'Connell for fruitful discussions and P. Hill and R. Armitage for technical support. The work presented herein was funded by the Engineering and Physical Sciences Research Council

(EPSRC), grant reference number: EP/m508196/1.

References

[1] I. Adamovich, S. D. Baalrud, A. Bogaerts, P. J. Bruggeman, M. Cappelli, V. Colombo, U. Czarnetzki, U. Ebert, J. G. Eden, P. Favia, D. B. Graves, S. Hamaguchi, G. Hieftje, M. Hori, I. D. Kaganovich, U. Kortshagen, M. J. Kushner, N. J. Mason, S. Mazouffre, S. Mededovic Thagard, H. R. Metelmann, A. Mizuno, E. Moreau, A. B. Murphy, B. A. Niemira, G. S. Oehrlein, Z. Lj Petrovic, L. C. Pitchford, Y. K. Pu, S. Rauf, O. Sakai, S. Samukawa, S. Starikovskaia, J. Tennyson, K. Terashima, M. M. Turner, M. C.M. Van De Sanden, and A. Vardelle. The 2017 Plasma Roadmap: Low temperature plasma science and technology. *Journal of Physics D: Applied Physics*, 50(32): 323001, 2017. ISSN 13616463. doi:10.1088/1361-6463/aa76f5.

[2] T. Lafleur and J.-P. Booth. Control of the ion flux and ion energy in CCP discharges using non-sinusoidal voltage waveforms. *Journal of Physics D: Applied Physics*, 45(39):395203, 2012. ISSN 0022-3727. doi:10.1088/0022-3727/45/39/395203.

[3] L. Bárdoš. Radio frequency hollow cathodes for the plasma processing technology. *Surface and Coatings Technology*, 86-87(PART 2):648–656, 1996. ISSN 02578972. doi:10.1016/S0257-8972(96)03056-3.

[4] S. J. Doyle, T. Lafleur, A. R. Gibson, P. Tian, M. J. Kushner, and J. Dedrick. Enhanced control of the ionization rate in radio-frequency plasmas with structured electrodes via tailored voltage waveforms. *Plasma Sources Science and Technology*, 26:125005, 2017. doi:10.1088/1361-6595/aa96e5.

[5] S. Dixon, C. Charles, R. W. Boswell, W. Cox, J. Holland, and R. Gottscho. Interactions between arrayed hollow cathodes. *Journal of Physics D: Applied Physics*, 46(14):145204, 2013. ISSN 0022-3727. doi:10.1088/0022-3727/46/14/145204.

[6] K. J. Kanarik, T. Lill, E. A. Hudson, S. Sriraman, S. Tan, J. Marks, V. Vahedi, and R. A. Gottscho. Overview of atomic layer etching in the semiconductor industry. *Journal of Vacuum Science & Technology A: Vacuum, Surfaces, and Films*, 33(2):020802, 2015. ISSN 0734-2101. doi:10.1116/1.4913379.

[7] C. Charles, W. Liang, L. Raymond, J. Rivas-Davila, and R. W. Boswell. Vacuum Testing of a Miniaturized Switch Mode Amplifier Powering an Electrothermal Plasma Micro-Thruster. *Frontiers in Physics*, 5(August):1–8, 2017. ISSN 2296-424X. doi:10.3389/fphy.2017.00036.

[8] S. Mazouffre. Electric propulsion for satellites and spacecraft: established technologies and novel approaches. *Plasma Sources Science and Technology*, 25(3):033002, 2016. ISSN 0963-0252. doi:10.1088/0963-0252/25/3/033002.

[9] R. A. Arakoni, J. J. Ewing, and M. J. Kushner. Microdischarges for use as microthrusters: modelling and scaling. *Journal of Physics D: Applied Physics*, 41(10):105208, 2008. ISSN 0022-3727. doi:10.1088/0022-3727/41/10/105208.

[10] D. O'Connell, R. Zorat, A. R. Ellingboe, and M. M. Turner. Comparison of measurements and particle-in-cell simulations of ion energy distribution functions in a capacitively coupled radio-frequency discharge. *Physics of Plasmas*, 14(10), 2007. ISSN 1070664X. doi:10.1063/1.2795634.

[11] S. Samukawa, M. Hori, S. Rauf, K. Tachibana, P. Bruggeman, G. Kroesen, J. C. Whitehead, A. B. Murphy, A. F. Gutsol, S. Starikovskaia, U. Kortshagen, J.-P. Boeuf, T. J. Sommerer, M. J. Kushner, U. Czarnetzki, and

N. Mason. The 2012 Plasma Roadmap. *Journal of Physics D: Applied Physics*, 45(25):253001, 2012. ISSN 0022-3727. doi:10.1088/0022-3727/45/25/253001.

[12] E. Schüngel, S. Mohr, J. Schulze, U. Czarnetzki, and M. J. Kushner. Ion distribution functions at the electrodes of capacitively coupled high-pressure hydrogen discharges. *Plasma Sources Science and Technology*, 23(1):015001, 2013. ISSN 09630252. doi:10.1088/0963-0252/23/1/015001.

[13] A. Perret, P. Chabert, J. Jolly, and J. P. Booth. Ion energy uniformity in high-frequency capacitive discharges. *Applied Physics Letters*, 86(2):10–13, 2005. ISSN 00036951. doi:10.1063/1.1848183.

[14] Ch. Wild and P. Koidl. Structured ion energy distribution in radio frequency glow-discharge systems. *Applied Physics Letters*, 54(6):505–507, 1989. ISSN 00036951. doi:10.1063/1.100913.

[15] J. Liu, G. L. Huppert, and H. H. Sawin. Ion bombardment in rf plasmas. *Journal of Applied Physics*, 68(8): 3916–3934, 1990. ISSN 00218979. doi:10.1063/1.346278.

[16] A. Manenschijn, G. C.A.M. Janssen, E. Van Der Drift, and S. Radelaar. Measurement of ion impact energy and ion flux at the rf electrode of a parallel plate reactive ion etcher. *Journal of Applied Physics*, 69(3):1253–1262, 1991. ISSN 00218979. doi:10.1063/1.347311.

[17] Ch. Wild and P. Koidl. Ion and electron dynamics in the sheath of radio-frequency glow discharges. *Journal of Applied Physics*, 69(5):2909–2922, 1991. ISSN 00218979. doi:10.1063/1.348601.

[18] W. C. Chen, X. M. Zhu, S. Zhang, and Y. K. Pu. Reconstruction of ion energy distribution function in a capacitive rf discharge. *Applied Physics Letters*, 94(21):211503, 2009. ISSN 00036951. doi:10.1063/1.3147216.

[19] S. Sharma, A. Sen, N. Sirse, M. M. Turner, and A. R. Ellingboe. Plasma density and ion energy control via driving frequency and applied voltage in a collisionless capacitively coupled plasma discharge. *Physics of Plasmas*, 25(8): 080705, 2018. ISSN 1070-664X. doi:10.1063/1.5045816.

[20] J. T. Gudmundsson, D. I. Snorrason, and H. Hannesdottir. The effect of pressure and driving frequency on electron heating in a capacitively coupled oxygen discharge. *Plasma Source Sciences and Technologies*, 27:025009, 2018. doi:10.1088/0963-0252/24/2/024002.

[21] A. Agarwal, S. Rauf, and K. Collins. Gas heating mechanisms in capacitively coupled plasmas. *Plasma Sources Science and Technology*, 21:055012, 2012. ISSN 0963-0252. doi:10.1088/0963-0252/21/5/055012.

[22] S. J. Doyle, A. R. Gibson, J. Flatt, T. S. Ho, R. W. Boswell, C. Charles, P. Tian, M. J. Kushner, and J. Dedrick. Spatio-temporal plasma heating mechanisms in a radio-frequency electrothermal microthruster. *Plasma Sources Science and Technology*, 27:085011, 2018. doi:10.1088/1361-6595/aad79a.

[23] C. Charles and R. W. Boswell. Measurement and modelling of a radiofrequency micro-thruster. *Plasma Sources Science and Technology*, 21(2):022002, 2012. ISSN 0963-0252. doi:10.1088/0963-0252/21/2/022002.

[24] C. Charles, J. Dedrick, R. W. Boswell, D. O'Connell, and T. Gans. Nanosecond optical imaging spectroscopy of an electrothermal radiofrequency plasma thruster plume. *Applied Physics Letters*, 103(12):124103, 2013. ISSN 00036951. doi:10.1063/1.4821738.

[25] A. Greig, C. Charles, N. Paulin, and R. W. Boswell. Volume and surface propellant heating in an electrothermal radio-frequency plasma micro-thruster. *Applied Physics Letters*, 105(5):054102, 2014. ISSN 0003-6951. doi:10.1063/1.4892656.

[26] A. Greig, C. Charles, and R. W. Boswell. Simulation of main plasma parameters of a cylindrical asymmetric capacitively coupled plasma micro-thruster using computational fluid dynamics. *Frontiers in Physics*, 2(January): 1–9, 2015. ISSN 2296-424X. doi:10.3389/fphy.2014.00080.

[27] T. S. Ho, C. Charles, and R. W. Boswell. A Comprehensive Cold Gas Performance Study of the Pocket Rocket Radiofrequency Electrothermal Microthruster. *Frontiers in Physics*, 4(January):1–16, 2017. ISSN 2296-424X. doi:10.3389/fphy.2016.00055.

[28] T. S. Ho, C. Charles, and R. Boswell. Neutral gas heating and ion transport in a constricted plasma flow. *Physics of Plasmas*, 24(8):8–13, 2017. ISSN 10897674. doi:10.1063/1.4996014.

[29] T. S. Ho, C. Charles, and R. W. Boswell. Performance modelling of plasma microthruster nozzles in vacuum. *Journal of Applied Physics*, 123(17):173301, 2018. ISSN 0021-8979. doi:10.1063/1.5012765.

[30] M. A. Lieberman and A. J. Lichtenberg. *Principles of Plasma Discharges and Materials Processing*. John Wiley & Sons, New Jersey, 2nd edition, 2005. ISBN 0-471-72001-1. doi:10.1002/0471724254.

[31] M.A. Lieberman. Analytical solution for capacitive RF sheath. *IEEE Transactions on Plasma Science*, 16(6): 638–644, 1988. ISSN 00933813. doi:10.1109/27.16552.

[32] C. Charles, R. Hawkins, and R. W. Boswell. Particle in cell simulation of a radiofrequency plasma jet expanding in vacuum. *Applied Physics Letters*, 106(9):093502, 2015. ISSN 0003-6951. doi:10.1063/1.4914109.

[33] T. Lafleur and R. W. Boswell. Particle-in-cell simulations of hollow cathode enhanced capacitively coupled radio frequency discharges. *Physics of Plasmas*, 19(2), 2012. ISSN 1070664X. doi:10.1063/1.3685709.

[34] A. Derzsi, I. Korolov, E. Schüngel, Z. Donkó, and J. Schulze. Effects of fast atoms and energy-dependent secondary electron emission yields in PIC/MCC simulations of capacitively coupled plasmas. *Plasma Sources Science and Technology*, 24(3):034002, 2015. ISSN 13616595. doi:10.1088/0963-0252/24/3/034002.

[35] M. J. Kushner. Hybrid modelling of low temperature plasmas for fundamental investigations and equipment design. *Journal of Physics D: Applied Physics*, 42(19):194013, 2009. ISSN 0022-3727. doi:10.1088/0022-3727/42/19/194013.

[36] S. J. Doyle, A. R. Gibson, R. W. Boswell, C. Charles, and J. P. Dedrick. Control of electron, ion and neutral heating in a radio-frequency electrothermal microthruster via dual-frequency voltage waveforms. *Plasma Sources Science and Technology*, 28(3):035019, 2019. doi:10.1088/1361-6595/ab0984.

[37] A. Salaba and R. P. Brinkmann. Non-neutral/quasi-neutral plasma edge definition for discharge models: A numerical example for dual frequency hydrogen capacitively coupled plasmas. *Japanese Journal of Applied Physics, Part 1: Regular Papers and Short Notes and Review Papers*, 45(6 A):5203–5206, 2006. ISSN 00214922. doi:10.1143/JJAP.45.5203.

[38] P. Tian and M. J. Kushner. Controlling VUV photon fluxes in low-pressure inductively coupled plasmas. *Plasma Sources Science and Technology*, 24:34017, 2015. ISSN 0963-0252. doi:10.1088/0963-0252/24/3/034017.

[39] M. Hayashi. Report No. IPPJ-AM-19. Technical report, Nagoya Institute of Technology, 1991.

[40] K. Tachibana. Excitation of the $1s_5$, $1s_4$, $1s_3$ and $1s_2$ levels of argon by low-energy electrons. *Physical Review A*, 34(2):451, 1986. doi:10.1103/PhysRevA.34.1007.

[41] D. Rapp and P. EnglanderGolden. Total Cross Sections for Ionization and Attachment in Gases by Electron Impact. I. Positive Ionization. *The Journal of Chemical Physics*, 43(5):1464–1479, 1965. ISSN 0021-9606. doi:10.1063/1.1696957.

[42] N. A. Dyatko, Y. Z. Ionikh, I. V. Kochetov, D. L. Marinov, A. V. Meshchanov, A. P. Napartovich, F. B. Petrov, and S. A. Starostin. Experimental and theoretical study of the transition between diffuse and contracted. *Journal of Physics D: Applied Physics*, 41:055204, 2008. doi:10.1088/0022-3727/41/5/055204.

[43] A. Bogaerts, R. G. V. Serikov, and V. V. Serikov. Calculation of gas heating in direct current argon glow discharges. *Journal of Applied Physics*, 87:8334, 1999. doi:10.1063/1.373545.

[44] H. W. Ellis, R. Y. Pai, E. W. McDaniel, E. A. Mason, and L. A. Viehland. Transport Properties of Gaseous Ions Over a Wide Energy Range. *Atomic Data and Nuclear Data Tables*, 17(3):177–210, 1976. doi:10.1016/0092-640X(76)90001-2.

[45] T. Gans, C. C. Lin, V. Schulz-von der Gathen, and H. F. Döbele. Phase-resolved emission spectroscopy of a hydrogen rf discharge for the determination of quenching coefficients. *Physical Review A*, 67:12707, 2003. ISSN 1050-2947. doi:10.1103/PhysRevA.67.012707.

[46] T. Gans, D. O'Connell, V. Schulz-von der Gathen, and J. Waskoenig. The challenge of revealing and tailoring the dynamics of radio-frequency plasmas. *Plasma Sources Science and Technology*, 19(3):034010, 2010. ISSN 0963-0252. doi:10.1088/0963-0252/19/3/034010.

[47] S. Siepa and U. Czarnetzki. Line integration and spatial resolution in optical imaging of plasmas. *Journal of Physics D: Applied Physics*, 48:385201, 2015. doi:10.1088/0022-3727/48/38/385201.

[48] J. Schulze, Z. Donkó, B. G. Heil, D. Luggenhölscher, T. Mussenbrock, R. P. Brinkmann, and U. Czarnetzki. Electric field reversals in the sheath region of capacitively coupled radio frequency discharges at different pressures. *Journal of Physics D: Applied Physics*, 41(10):105214, 2008. ISSN 15735052. doi:10.1007/s11258-017-0772-4.

[49] A. V. Phelps and Z. Lj. Petrovic. Cold-cathode discharges and breakdown in argon: surface and gas phase production of secondary electrons. *Plasma Sources Science and Technology*, 8(3):R21–R44, 1999. ISSN 0963-0252. doi:10.1088/0963-0252/8/3/201.

[50] J. Schulze, E. Schüngel, Z. Donkó, D. Luggenhölscher, and U. Czarnetzki. Phase resolved optical emission spectroscopy: a non-intrusive diagnostic to study electron dynamics in capacitive radio frequency discharges. *Journal of Physics D: Applied Physics*, 43(12):124016, 2010. ISSN 0022-3727. doi:10.1088/0022-3727/43/12/124016.

[51] J. Schulze, Z. Donkó, T. Lafleur, S. Wilczek, and R. P. Brinkmann. Spatio-temporal analysis of the electron power absorption in electropositive capacitive RF plasmas based on moments of the Boltzmann equation. *Plasma Sources Science and Technology*, 27(5):055010, 2018. ISSN 13616595. doi:10.1088/1361-6595/aabebc.

[52] A. R. Gibson, Z. Donkó, L. Alelyani, L. Bischoff, G. Hübner, J. Bredin, S. J. Doyle, I. Korolov, K. Niemi, T. Mussenbrock, P. Hartmann, J. P. Dedrick, J. Schulze, T. Gans, and D. O'Connell. Disrupting the spatio-temporal symmetry of the electron dynamics in atmospheric pressure plasmas by voltage waveform tailoring. *Plasma Sources Science and Technology*, 28:01LT01, 2019. doi:10.1088/1361-6595/aaf535.

[53] V. Godyak, R. Piejak, and B Alexandrovich. Measurements of electron energy distribution in low-pressure R F discharges. *Plasma Sources Science and Technology*, 1(1):36–58, 1992. doi:10.1088/0963-0252/1/1/006.

[54] A. V. Phelps. The application of scattering cross sections to ion flux models in discharge sheaths. *Journal of Applied Physics*, 76(2):747–753, 1994. ISSN 00218979. doi:10.1063/1.357820.

[55] M. J. Kushner. Distribution of ion energies incident on electrodes in capacitively coupled rf discharges. *Journal of Applied Physics*, 58(11):4024–4031, 1985. ISSN 00218979. doi:10.1063/1.335580.